On the Challenges of Tomography Retrievals of a 2D Water Vapor Field Using Ground-Based Microwave Radiometers: An Observation System Simulation Experiment

VÉRONIQUE MEUNIER

Department of Atmospheric and Oceanic Sciences, McGill University, Montreal, Quebec, Canada

DAVID D. TURNER

National Oceanic and Atmospheric Administration/National Severe Storms Laboratory, Norman, Oklahoma

PAVLOS KOLLIAS

Department of Atmospheric and Oceanic Sciences, McGill University, Montreal, Quebec, Canada

(Manuscript received 5 September 2013, in final form 8 October 2014)

ABSTRACT

Two-dimensional water vapor fields were retrieved by simulated measurements from multiple ground-based microwave radiometers using a tomographic approach. The goal of this paper was to investigate how the various aspects of the instrument setup (number and spacing of elevation angles and of instruments, number of frequencies, etc.) affected the quality of the retrieved field. This was done for two simulated atmospheric water vapor fields: 1) an exaggerated turbulent boundary layer and 2) a simplified water vapor front. An optimal estimation algorithm was used to obtain the tomographic field from the microwave radiometers and to evaluate the fidelity and information content of this retrieved field.

While the retrieval of the simplified front was reasonably successful, the retrieval could not reproduce the details of the turbulent boundary layer field even using up to nine instruments and 25 elevation angles. In addition, the vertical profile of the variability of the water vapor field could not be captured. An additional set of tests was performed using simulated data from a Raman lidar. Even with the detailed lidar measurements, the retrieval did not succeed except when the lidar data were used to define the a priori covariance matrix. This suggests that the main limitation to obtaining fine structures in a retrieved field using tomographic retrievals is the definition of the a priori covariance matrix.

1. Introduction

High-resolution water vapor field measurements are needed for boundary layer and cloud life cycle research. For convection studies, most measurement technologies are challenged by the requirements stated by Weckwerth et al. (1999) in spatial resolution (up to 100 m in the vertical and 300 m in the horizontal) and in temporal resolution (10 min), even if the latter is clearly insufficient in the context of the stated horizontal resolution. For boundary layer (BL) studies, resolution requirements are 10 times higher (Hardesty and Hoff 2012). To meet these challenging needs, it becomes necessary to optimally combine the measurements of multiple instruments.

Water vapor fields can be measured using both active (lidars, radar refractivity) and passive (microwave radiometers, infrared spectrometers) remote sensors. Lidars are the most accurate remote sensors for measuring water vapor with accuracies around 5% (Hardesty and Hoff 2012; Wulfmeyer and Bösenberg 1998; Turner and Goldsmith 1999), but they are very expensive instruments. The passive instruments are more affordable, but in general they provide more range-limited measurements. For instance, Schween et al. (2011) used a single fully scanning microwave radiometer (MWR) to

Corresponding author address: Véronique Meunier, Department of Atmospheric and Oceanic Sciences, McGill University, Burnside Hall, Room 945, 805 Sherbrook Street West, Montreal QC H3A 0B9, Canada.
E-mail: veronique.meunier2@mcgill.ca

DOI: 10.1175/JTECH-D-13-00194.1

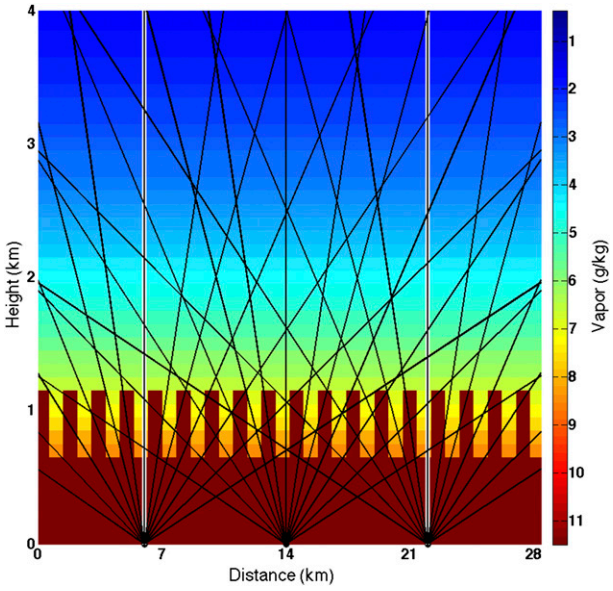

FIG. 1. Sketch of a three-radiometer tomographic set up in a planar (height vs distance) atmosphere with the alternating blob atmospheric field. Each instrument scans 13 elevation angles (black lines). Statistics computed in this study are computed for the region inside the two vertical white bars for the full height of the atmosphere, which reaches 7 km, but only the first 4 km are shown.

measure a 3D field of water vapor with low temporal resolution (18 min) and spatial resolution (every 10°).

Using several MWRs measuring the same atmospheric humidity field, and combining the measurements from the various instruments, should provide better spatial resolution compared to the single instrument. When several of the same passive instruments are used, their measurements can be combined to increase the constraints on the field where the instruments scan through the same area (Fig. 1). This permits the measurement of an extra dimension that a single path-integrated measurement could not achieve. This is the basis of the tomographic technique. Tomography has been used in meteorology first for satellite measurements (Fleming 1982) and then for a global positioning system network (Bevis et al. 1992). It has been used in microwave radiometry to derive 3D clouds using both ground-based (Huang et al. 2008; Warner et al. 1985, 1986) and aircraft-based (Drake and Warner 1988; Bobylev 1997; Huang et al. 2010) measurements.

In comparison to tomography, instrument synergy uses different instruments and combines their measurements in order to reduce their limitations and combine their strengths. The synergy can also be used to get a better picture of the atmosphere as a whole. By combining instruments that measure very different atmospheric parameters, complementary information can be provided to better understand an atmospheric situation (Han and Westwater 1995; Crewell and Löhnert 2003; Löhnert et al. 2004). Active remote sensors such as Raman lidars (RLs) are able to provide high-vertical-resolution measurements of water vapor, albeit typically only directly above the instrument (Goldsmith et al. 1998; Turner et al. 2000; Han et al. 1994). RLs measure profiles of water vapor in time, with a time resolution in the BL of 1 min or less (Ferrare et al. 2006; Wulfmeyer et al. 2010). Thus, combining the vertical profile observations from a RL with the scanning MWR brightness temperature observations could help the tomographic retrieval constrain the vertical and horizontal distribution of water vapor in and just above the BL better than using only MWRs.

How well can ground-based instruments retrieve water vapor fields at a resolution comparable to those needed for convection and BL research? Padmanabhan et al. (2009) claim to have retrieved 3D water vapor patterns by tomography with a resolution of 500 m in the horizontal and 500–1000 m in the vertical, but verification remains difficult. To make this verification, an observation system simulation experiment (Masutani et al. 2010) has been used to evaluate the use of tomography to derive water vapor fields (Padmanabhan et al. 2009; Steinke et al. 2014). For example, Steinke et al. (2014) used a large-eddy simulation model to investigate the improvement of using a tomographic retrieval of water vapor using two radiometers to retrieve a 2D water vapor field compared to the use of a single radiometer. They found that using two radiometers in the tomographic solution improved the information content of the retrieval of the water vapor field by 61% compared to only using a single radiometer.

The object of our study is to determine retrieval accuracy, particularly in the BL, and to evaluate how sensitive the solution is to changes in instruments and their scanning strategy. For this study, we use an observation system simulation experiment to quantify the change in accuracy of a retrieved 2D water vapor field following changes in tomographic parameters. In addition, this study will also evaluate the benefit of using instrument synergy between active and passive remote sensors in order to improve the accuracy and information content in the tomographic retrieval 2D water vapor field. We will evaluate the accuracy of a retrieved 2D water vapor field measured using microwave radiometer tomography as did Steinke et al. (2014), but we will be using an a priori covariance matrix that does not come directly from the field because in reality we do not have this information.

2. Retrieval simulation setup

a. *Atmospheric fields*

For this study, we have created two simulated atmospheric fields in order to examine the performance of

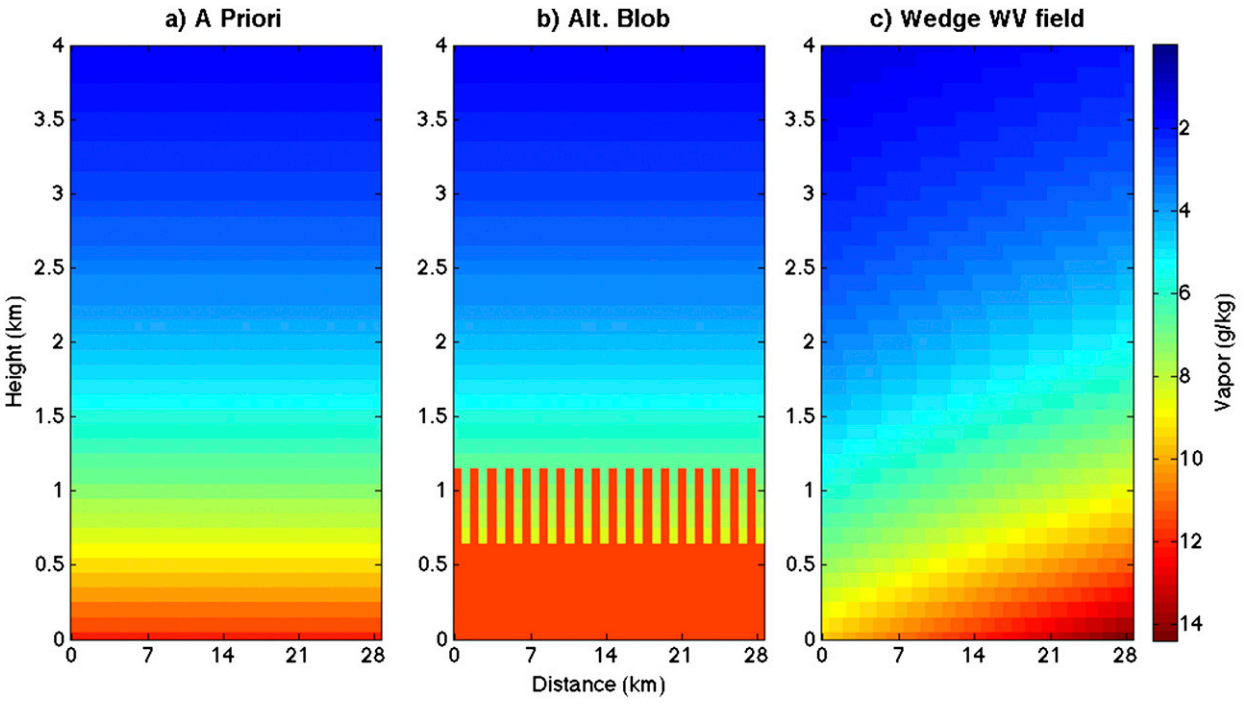

FIG. 2. Water vapor atmospheric fields used in this study (in mixing ratio) for (a) the a priori, (b) the alternating blobs at the top of the BL truth field representing a developed afternoon BL, and (c) the wedge truth field representing a frontal boundary.

microwave water vapor tomography. We assumed simple vertically stratified and horizontally homogeneous temperature and pressure fields, and cloud-free conditions. The temperature vertical profile is a constant lapse rate ($6.5\,\mathrm{K\,km^{-1}}$), and the pressure is exponentially decaying with a scale height of

$$H = \frac{g}{R_p T_v}, \tag{1}$$

where g is the gravitational acceleration, R_p is the individual gas constant for air ($287\,\mathrm{J\,kg^{-1}\,K^{-1}}$), and T_v is the virtual temperature. The temperature and pressure fields are the same for all these atmospheres and are assumed to be known in all cases, since we are focusing on the measurement of water vapor.

The only parameter that is changing between atmospheres is the water vapor field. For the a priori atmosphere, the water vapor is exponentially decaying with a scale height of 2 km (Fig. 2a) unless otherwise stated. Two water vapor fields (used as true or observed fields) were created to reflect different BL conditions. The first field, called the ''alternating blob'' field, represents a well-mixed BL with exaggerated billows at the top of the BL (here set at 1 km). The alternating blobs at the BL top are 800 m in the horizontal and 200 m in the vertical and are continuously alternating between the BL values and the free-tropospheric values (Fig. 2b). It should be noted that the placement of the blobs are nonsymmetrical to the center of the field. The second truth field, called the ''wedge'' pattern, represents the passage of a water vapor front (e.g., dryline or front) coming over the region (Fig. 2c). The vertical grid resolution is 100 m and the horizontal grid is 400 m for all of these atmospheres following the requirements set by the Hardesty and Hoff (2012) and Weckwerth et al. (1999) reports mentioned in the introduction. The maximum horizontal extent is 28.8 km and the vertical extent is 7 km.

Computing limitations forced us to restrict our analysis to two atmospheric fields. We purposefully chose to use synthetic atmospheres in an attempt to be better able to observe how the solution will converge when increasing the number of measurements, as we want to characterize how the tomography retrieval performs. This would have been more difficult with a real field.

b. *Retrieval algorithm*

To perform the water vapor retrieval using the microwave radiometers and to get a quantitative evaluation of the retrieval accuracy, a commonly used optimal estimation algorithm was chosen for this study. This optimal estimation algorithm, based on Rodgers (2000), was done using the iterative equation

$$\mathbf{X}_{i+1} = \mathbf{X}_a + \mathbf{S}_a\mathbf{K}_i^{\mathrm{T}}(\mathbf{K}_i\mathbf{S}_a\mathbf{K}_i^{\mathrm{T}} + \mathbf{S}_\varepsilon)^{-1}[\mathbf{Y} - F(\mathbf{X}_i) + \mathbf{K}_i(\mathbf{X}_i - \mathbf{X}_a)], \quad (2)$$

where i is the iteration, T is the transpose of the matrix, $\mathbf{X}_{i+1}$ is the new guess of the atmospheric state, $\mathbf{X}_a$ is the a priori atmospheric state, $\mathbf{S}_a$ is the a priori covariance matrix, $\mathbf{K}_i$ is the Jacobian matrix for the current iteration, $\mathbf{S}_\varepsilon$ is the observation error covariance matrix, $\mathbf{Y}$ is the observation matrix, $\mathbf{X}_i$ is the current atmospheric state (or for the first iteration it is the a priori), and $F(\,)$ is the forward model.

Simulated MWR observations were computed by driving the forward model with the water vapor profile from the field along the instrument's view direction and then adding normally distributed random noise to the calculation. MWR "observations" at different frequencies, locations, and elevation angles were used as the observation vector $\mathbf{Y}$.

The Jacobian matrix $\mathbf{K}$ was calculated for each iteration of Eq. (2). The calculation of the Jacobian matrix was done by perturbing each element of $\mathbf{X}_i$ by 5% and using the forward model to calculate the effect this perturbation will have in brightness temperature (TB) such as

$$\mathbf{K}_i = \frac{\partial \mathbf{Y}}{\partial \mathbf{X}_i} = \frac{\partial F(\mathbf{X}_i)}{\partial \mathbf{X}_i} \approx \frac{F(1.05\mathbf{X}_i) - F(\mathbf{X}_i)}{0.05\mathbf{X}_i}. \quad (3)$$

The Jacobian matrix was calculated using a positive perturbation only (one-sided approach). This was done to save calculation time and did not affect significantly the accuracy given that $\mathbf{K}$ varies slowly with $\mathbf{X}_i$ (i.e., the forward model is nearly linear in the cloud-free atmospheres for the frequencies used in this study).

The observation error covariance matrix $\mathbf{S}_\varepsilon$ was a diagonal matrix with the instrument's error variance on the diagonal elements. The instrument's error used in this study was chosen to be 0.7 K for all instruments, frequencies, and elevation angles. The $\mathbf{S}_\varepsilon$ used assumed independent measurement errors between channels, elevation angles, and instruments. We will evaluate the impact on the results of various random error levels in a later part of this paper.

We assumed that the specifics of the field were not known, as it would be the case for real measurements, and as such, the a priori covariance matrix $\mathbf{S}_a$ was defined as

$$\mathbf{S}_a(n_1, p_1, n_2, p_2) = \boldsymbol{\sigma}(n_1, p_1)\boldsymbol{\sigma}(n_2, p_2)\mathbf{corr}_{\mathrm{nn}}(n_1, n_2)\mathbf{corr}_{\mathrm{pp}}(p_1, p_2), \quad (4)$$

where (n_1, p_1) and (n_2, p_2) are the horizontal (n) and vertical (p) coordinates of two points, $\boldsymbol{\sigma}$ is the point error, $\mathbf{corr}_{\mathrm{nn}}$ is the horizontal correlation, and $\mathbf{corr}_{\mathrm{pp}}$ is the height correlation. The $\boldsymbol{\sigma}$ and $\mathbf{corr}_{\mathrm{pp}}$ were calculated using 5 years of radiosondes (2005–10) from the U.S. Department of Energy's Atmospheric Radiation Measurement Program Southern Great Plains site (ARM SGP) (north-central Oklahoma) (Stokes and Schwartz 1994) for the months of May and June during which our two classes of simulated atmospheric fields (frontal passages and turbulent boundary layers) are both prevalent. The 1357 soundings used were interpolated to the vertical levels used in the simulated atmospheres. From these soundings, a standard deviation was computed for each height level (σ) and so was the vertical correlation ($\mathbf{corr}_{\mathrm{pp}}$) between different height levels. The horizontal correlation matrix ($\mathbf{corr}_{\mathrm{nn}}$) was created using an exponential equation assuming a set correlation distance:

$$\mathbf{corr}_{\mathrm{nn}}(n_1, n_2) = e^{[-|x(n_1) - x(n_2)|/D}, \quad (5)$$

where D is the horizontal correlation distance, and x is the horizontal distance of each of the two points with horizontal coordinates n_1 and n_2. The exponential was used because errors in atmospheric fields often show an exponential correlation dependence with distance. The value for D used in this study was 13.5 km unless otherwise specified. The 13.5-km correlation distance was chosen for the main analysis, but in section 3c several different correlation distances are examined. A second method to construct the $\mathbf{S}_a$ matrix using RL measurements will be discussed in section 4c.

c. Metrics of evaluation

The optimal estimation algorithm formulation provides several quantitative metrics that can be used to evaluate the accuracy and performance of the retrieval. The degrees of freedom for signal (DFS) were used here as a measure of information contained in the retrieval's solution. The total DFS was defined as

$$\mathrm{DFS} = \mathrm{tr}[\mathbf{S}_a\mathbf{K}_i^{\mathrm{T}}(\mathbf{K}_i\mathbf{S}_a\mathbf{K}_i^{\mathrm{T}} + \mathbf{S}_\varepsilon)^{-1}\mathbf{K}_i], \quad (6)$$

where tr is the trace of the matrix and i is still the iteration as in Eqs. (2) and (3) (Rodgers 2000). The DFS provided the real number of observations (i.e., independent pieces of information in a measurement) used to constrain the retrieval algorithm. The total possible DFS for both atmospheric fields was 2911 (71 vertical points times 41 horizontal points). In addition to the DFS, the root-mean-square difference (RMSD) of the solution with respect to the truth was also calculated for each retrieval solution. This was used to evaluate the accuracy of the retrieval's solutions.

The statistics used in this study (DFS and RMSD) were computed in the region of the atmosphere included between the radiometers (i.e., between 6.4 and 22.4 km in the horizontal direction for heights between 0 and 7 km) where it is of interest for tomographic measurements. The calculation of the DFS would be correct if and only if the path followed by the radiation arriving at the MWR had been entirely contained within the analysis field where $\mathbf{S}_a$ was defined. Many paths from off-zenith measurement go off the edge of the domain, where $\mathbf{S}_a$ and $\mathbf{K}$ are undefined, resulting in biases in information calculation for columns on the edge of the domain. Therefore, we chose not to consider their value in our statistics calculation.

3. Evaluation of the radiometric setup on the tomographic retrieval results

We start by examining the impact of the different characteristics of the MWR instrument setup used in the tomographic retrieval of the 2D water vapor fields. Here, we examine the effects of the number and spacing of the elevation angles, the number of frequencies used in each radiometer (i.e., profiling MWR vs nonprofiling MWR), the number of MWRs used in the tomographic retrieval, and the measurement accuracy (noise level) of the MWR. In addition, we also evaluate effects that the correlation distances used to create the $\mathbf{S}_a$ matrix have on the retrieval. For each of these configurations, the effects on the DFS and the different RMSDs have been examined.

a. Radiometer characteristics and setup

To perform the sensitivity study, some instrument parameters are required. We have chosen three sets of frequencies representing different MWRs: the Humidity and Temperature Profiler (HATPRO) radiometer (22.24, 23.04, 23.84, 25.44, 26.24, 27.84, 31.4 GHz) (Radiometer Physics GmbH 2011), the compact microwave radiometers (CMR) (22.12, 22.67, 23.25, 24.5 GHz) (Iturbide-Sanchez et al. 2007), and the traditional two-frequency radiometers (TRAD) (23.8, 31.4 GHz) (Turner et al. 2007; Cadeddu et al. 2013) water vapor channels. The HATPRO was chosen because of its ability to measure all its channels in parallel and, therefore, perform a relatively rapid scan. The CMR has been used in the past for tomographic measurements of water vapor (Padmanabhan et al. 2009). Since many weather centers and research programs use the two-channel radiometers, they are also included in this study. The real beamwidth and bandwidth of the instruments are not taken into account and are assumed to be delta functions. This was done to reduce the computation time required for these retrievals and to simulate perfect instruments, creating the ideal conditions for the tomographic retrieval.

Tomography requires many elevation angles to measure the water vapor field. We have selected three sets of the number of elevation angles: 13, 19, and 25 angles. These sets have been chosen such that a full scan can be performed within 1 min based on the fact that the HATPRO instrument needs 2 s per measurement to obtain a good reading in normal operation (1 s for integrating time and 1 s for calibration) (Radiometer Physics GmbH 2011). The final parameter tested was the sensitivity of the solution to the number of instruments and the distance between the instruments. In this study, we have chosen five sets of the number of instruments: one instrument, two instruments (spaced by 16 km), three instruments (spaced by 8 km), five instruments (spaced by 4 km), and nine instruments (spaced by 2 km). The instruments have been equally distributed horizontally in the atmospheric field.

b. Microwave radiometer forward model

The forward model used in this study for the MWRs is that of Meunier et al. (2013) with the Rosenkranz (1998) absorption model using the water vapor continuum correction found by Turner et al. (2009). We also tested our results using the Liebe (1989) absorption model and the differences were negligible. Tomography requires the MWR to scan at low-elevation angles in order to measure the lowest part of the atmosphere. At these low-elevation angles, the MWR beam does not follow a straight path. Therefore, the refractive index and its variation need to be known in order to properly determine the location of the MWR's view along its curved beam. Given that the Rosenkranz absorption code does not have an explicit calculation of the refractive index, the Bean and Dutton (1966) refractive index calculation is used. The Bean and Dutton refractive index is calculated following

$$n = 1 + \left(\frac{C_p P}{T} + \frac{C_w e}{T^2}\right) 10^{-6}, \tag{7}$$

where P is pressure (hPa), T is temperature (K), e is vapor pressure (hPa), and C_p and C_w are constants (C_p = 77.6 K hPa^{-1}, $C_w = 3.75 \times 10^5$ hPa K^{-2}). The difference between the Bean and Dutton refractive index and the full refractive index calculations using Liebe (1989) are also negligible.

c. Simulation experiments: Varying radiometer characteristics

Initially, the work focused on trying to determine the value of different measurement strategies, such as the

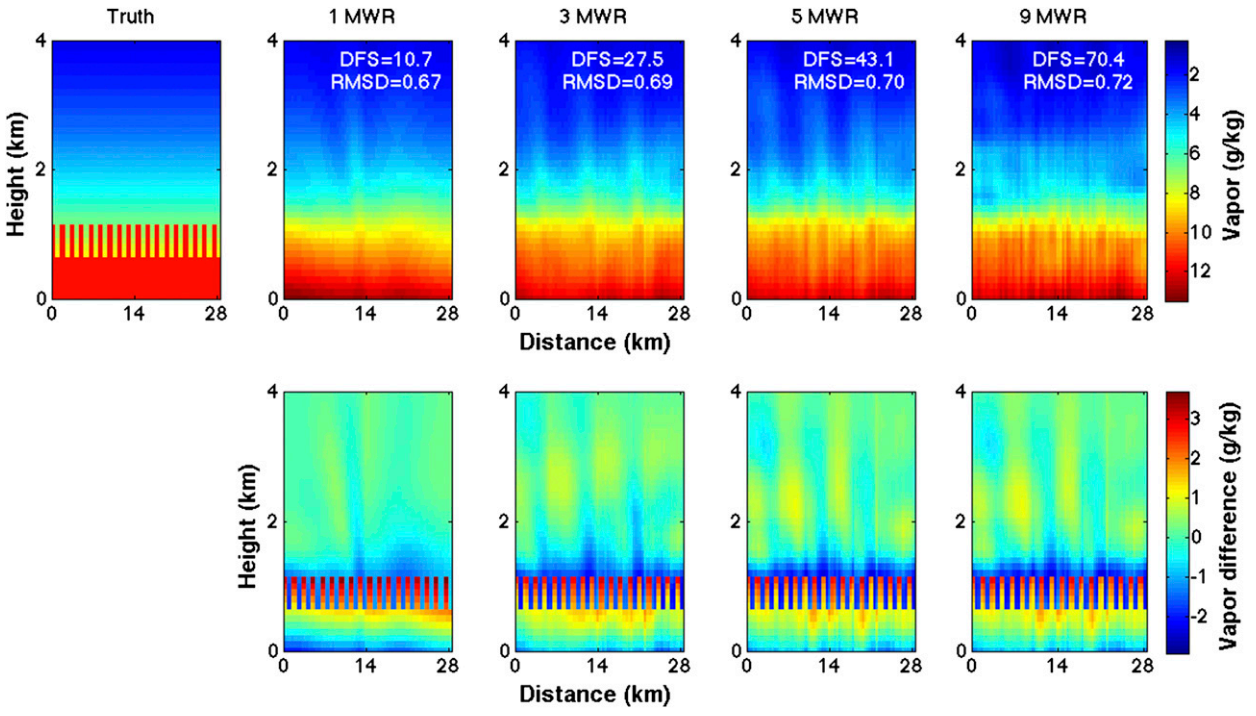

FIG. 3. (top) Comparison of retrieved fields for the alternating blob atmosphere between the true water vapor field and using one MWR, three MWRs, five MWRs, and nine MWRs for HATPRO radiometers with 25 elevation angles. (bottom) Difference between the solution and the truth fields for the same number of instruments as in the (top). The values of DFS and RMSD are noted in the retrieved field plots ($g\,kg^{-1}$).

number and spacing of elevation angles, the number and type of radiometer instruments, the instrument error, and finally, the horizontal and vertical correlation length of $\mathbf{S}_a$.

Using the DFS retrieved as a metric for retrieval fidelity, we found that the degree of sophistication of the radiometer (i.e., how many channels it has) played a minor role, with the seven-frequency HATPRO retrieving only 1.3 times more DFS than the two-frequency TRAD and 1.2 times more DFS than the four-frequency CMR. This effect is similar for the two water vapor fields used in this study. The additional frequencies provide the MWRs with the capacity of profiling the atmosphere. This is demonstrated in the amount of DFS each instrument obtains at zenith: the DFS right above the radiometers shows that the HATPRO frequencies have the largest DFS (2.0), whereas the CMR and TRAD have DFS values directly above them of 1.8 and 1.6, respectively. This DFS value at zenith for the HATPRO instrument agrees with earlier work by Löhnert et al. (2009), which found DFS values at zenith for HATPRO between 1.6 and 2.7. Despite the small contribution, the additional information that comes from the additional frequencies comes in range and hence helps contribute to the tomographic reconstruction.

We found that increasing the number of instruments increased the number of DFS in a linear manner for both atmospheric fields (Figs. 3 and 4, see numbers in the individual plots), with a factor of 6.6 improvement being achieved between the solutions that used one and nine instruments, while increasing from three to nine MWRs yields a factor of 2.6 increase of DFS and increasing from five to nine instruments increases the DFS by a factor of 1.6. However, the improvement in the DFS slowly approaches a limit as the number of instruments used in the retrieval is increased (Fig. 5a).

Increasing the number of angles also benefited the solution, as nearly doubling the number of angles from 13 to 25 yields a gain of a factor of 1.6 in DFS, while increasing the elevation angles from 19 to 25 angles improves the DFS by 1.2. These results show that if we already have many elevation angles, then further increasing the number of angles has diminishing returns compared to increasing the number of elevation angles from a small number of angles (Fig. 5b). Another issue with using many elevation angles is the time it takes to complete the scan. This will be particularly problematic for rapidly evolving atmospheres. The elevation spacing of the angles plays a small role in the retrieval. When many angles are used, spacing the angles equally in elevation yields higher DFS compared to more

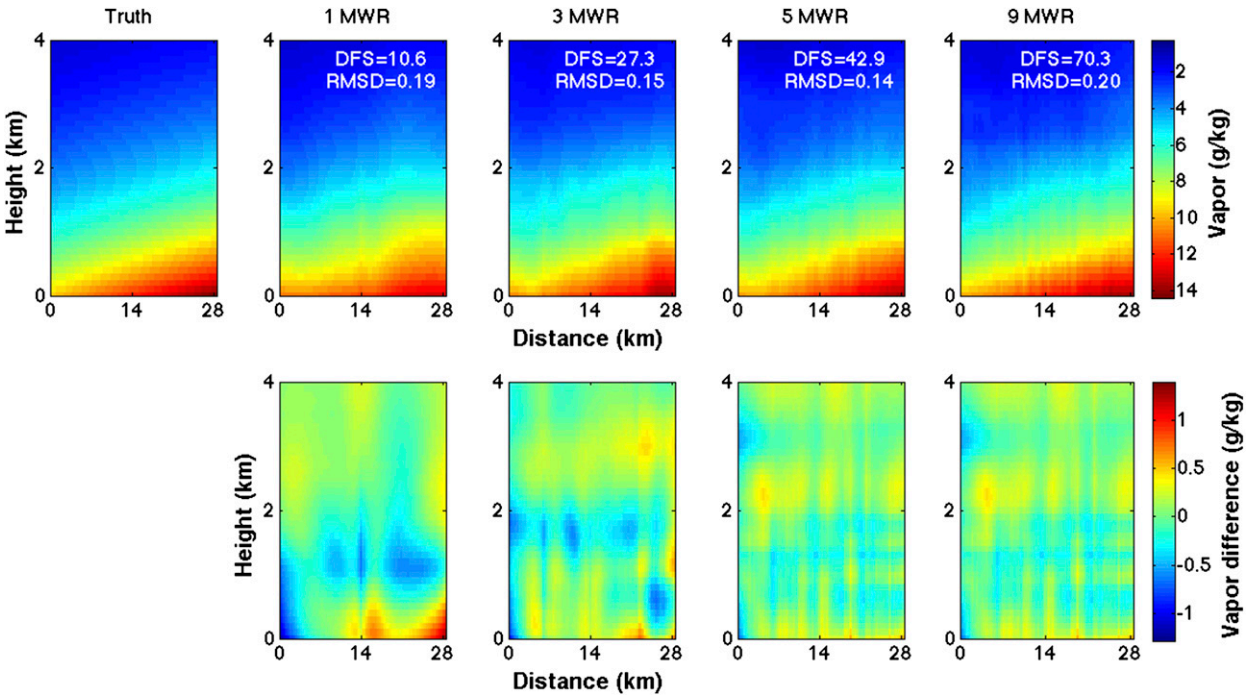

FIG. 4. As in Fig. 3, but for the wedge atmosphere.

sophisticated spacings when many angles are used. The ideal angular spacing will depend on the number of radiometers, the horizontal spacing of the instruments, and the height of the maximum variability of the water vapor field.

The measurement accuracy proved to have the smallest effect, a halving of the measurement error from 0.7 to 0.35 K only resulted in an 11% gain in DFS. However, the retrieval solutions are qualitatively insensitive to the change in measurement error with the spatial patterns of the solutions remaining unchanged for the range of noise levels tested. The results suggest that the retrieval benefits more from an increase in the number of ''path measurements'' (defined as the number of instruments times the number of elevation angles) than from an improvement in the radiometric precision of the measurement.

The most significant result proved to be that despite having what in practice would be a large number of sophisticated instruments (up to nine HATPRO MWRs) making measurements at many elevation angles (up to 25), the retrieval fidelity remained poor for the alternating blob atmosphere, as can be seen in Fig. 3 for nine instruments and 25 elevation angles. This is further highlighted by the RMSD between the solution and the retrieval (Fig. 6b): beyond a small number of path measurements, the accuracy of the field improves slowly, as if the retrieval algorithm could not efficiently use the additional measurements.

However, the information of the presence of structure in the water vapor field, even if the structures are not positioned exactly, is an important aspect of the field. Therefore, in order to evaluate if the retrieval is indeed

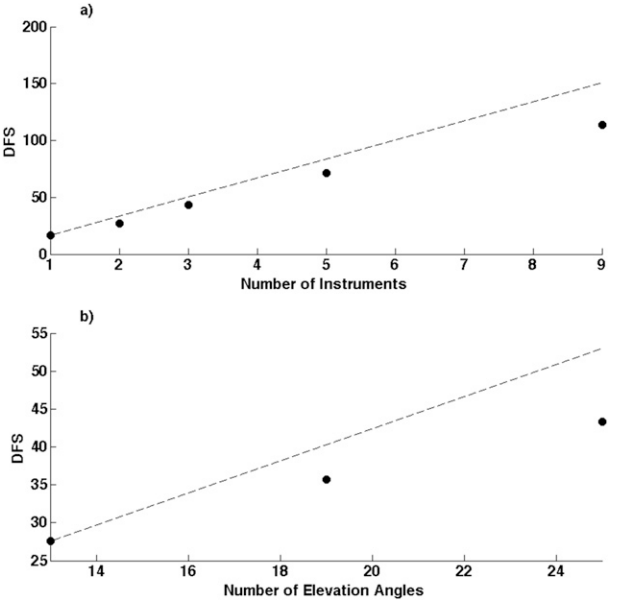

FIG. 5. DFS as a function of (top) number of instruments and (bottom) number of elevation angles. Dotted line starts at the origin and goes through the first point. In the absence of signal saturation, all points should be aligned on that line.

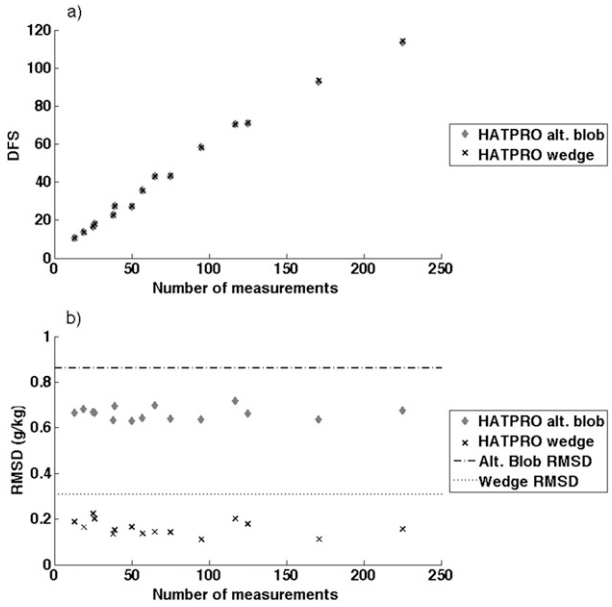

FIG. 6. Scatterplot of (a) DFS and (b) RMSD in mixing ratio between the solution and the observed atmospheric fields for both the alternating blob (gray diamonds) and the wedge (black Xs) for the HATPRO radiometer. Note that the DFS vs number of path measurements [(a)] is virtually the same for the two atmospheric fields. [(b)] In the RMSD plot, the dashed–dotted lines and the dotted lines are the RMSD between the truth and the a priori field for the alternating blob and for the wedge, respectively, while the scatterplot is the RMSD for the various configurations as mentioned previously. Number of path measurements is the number of instruments multiplied by the number of angles used by each radiometer.

recognizing this variability in the field, we looked at the variability of water vapor with height across the field for the alternating blob case and compared it to the retrieval's solution for the different number of instruments (Fig. 7a). This shows that increasing the number of measurements does help to capture some of the variability in the field. However, the altitude of the maximum variability of water vapor in the solution field is above the one seen in the true field. In addition, the magnitude of the maximum standard deviation is ~5 times smaller than the magnitude of the maximum standard deviation in the true field. This shows that although some of the variability can be retrieved, the tomographic measurements seem unable to capture the true magnitude of the variability at the top of the boundary layer correctly in this case. This may be caused by the correlation lengths (both vertical and horizontal) of the $\mathbf{S}_a$ matrix being too large. This being said, the depth of the boundary layer is reasonably well captured with respect to the true field and shows definitive improvement from the a priori (Fig. 7b). As the number of instruments increase, the mean water vapor profile becomes steeper and the kinks in the mean profile show up nicely.

The sensitivity of the retrieved field to the assumed horizontal and vertical correlations of the $\mathbf{S}_a$ matrix was tested. The horizontal correlation was changed from the originally assumed 13.5 km to 400 m, 2 km, 50 km, 100 km, and 200 km. For the alternating blob field, when the shortest horizontal correlation length (400 m) was used in the retrieval, the solution field resulted in many small-scale vertical plumes. As the horizontal correlation length increases, the plumes widen; when that horizontal correlation becomes too large (50 km and larger), the plumes disappear altogether and the field assumes a 1D structure (i.e., nearly plane parallel). The vertical plumes are caused by the relatively large vertical correlation that was incorporated into the $\mathbf{S}_a$ matrix from the soundings. We also varied the vertical correlation distance of the $\mathbf{S}_a$ matrix. When the vertical correlation distance of $\mathbf{S}_a$ was changed from the 4 km found from the 5 years of soundings to 400 m, and when one uses a horizontal correlation length of 400 m, the tomographic MWR measurements only change the a priori field along the paths where measurements are taken, and do not affect the a priori field beyond. Note that in the wedge case, using long horizontal correlation lengths is close to optimal, as the correlation in the atmospheric field is indeed larger for this case relative to the blob atmosphere. Thus, the $\mathbf{S}_a$ matrix has a very important effect on the retrieval's solution. For less variable fields, the larger horizontal correlation distance is less problematic, but for variable fields, like the alternating blob field, it is important to get an accurate $\mathbf{S}_a$ matrix. Similarly, in the vertical it is important that $\mathbf{S}_a$ has the altitude of the maximum variability approximately correct.

This raises an important factor about retrievals: the choice of $\mathbf{S}_a$. The success of retrieving a field is very sensitive to how accurate the $\mathbf{S}_a$ is for the particular case under study. For example, in this study, the correlation distances of $\mathbf{S}_a$ are better suited to the wedge than to the alternating blobs and, even though the use of tomography can add up to 120 new constraints (DFS), these new constraints cannot reduce the error on the 2911 locations (maximum possible DFS) in the field as effectively as they would if the $\mathbf{S}_a$ had the right correlation distances for the field considered. Taking the maximum DFS we have in this study, 120, and comparing it to the 2911 pixels in the field, which are 400 m $\times$ 100 m in size, we find that we have, on average, one constraint per 1.68 km^2. The ability to retrieve subkilometer structures therefore entirely relies on $\mathbf{S}_a$. When the $\mathbf{S}_a$ is inappropriate for the field, the information is not spread effectively in space and may potentially cause incompatible

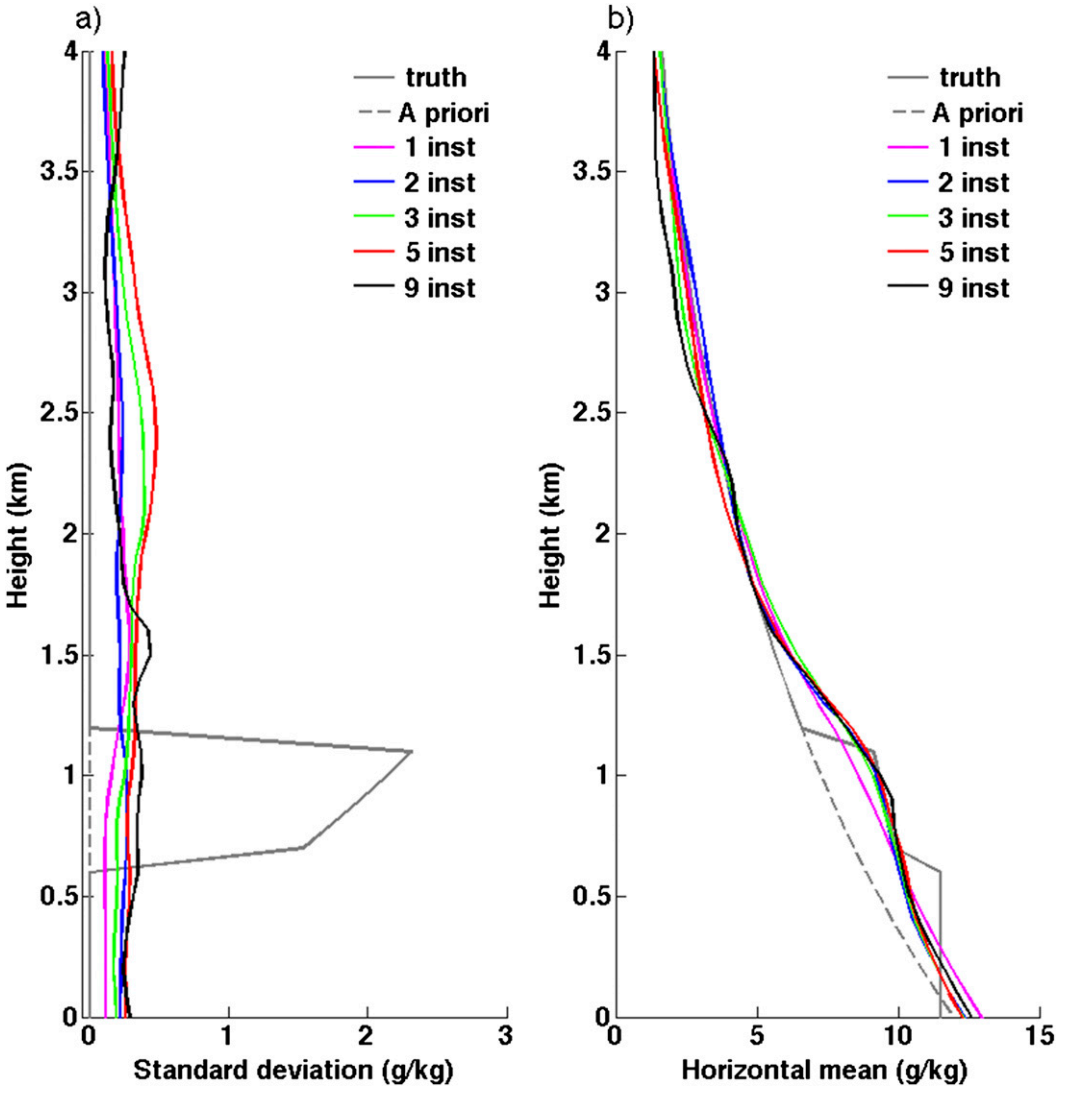

FIG. 7. Line plot of (a) the horizontal standard deviation and (b) the horizontal mean of water vapor with height for the alternating blobs water vapor field: true field (gray), a priori field (dashed gray), and the solution fields for the different number of instruments (colors). A priori standard deviation profile is zero at all heights.

measurements to compete with each other during the retrieval process. Therefore, it is important not only to have an $\mathbf{S}_a$ that is possible for the field, but one that is accurate for every particular field. To achieve this, additional information must be sought from other sources.

4. Impact of the Raman lidar on the tomographic retrieval results

The analysis of the results presented so far suggests the following: if we want to resolve the detailed structure of the BL, considering the large number of pixels in a 2D field and comparing that to the number of DFS that can be gained from measurements, the quantity of measurements (and the time needed to perform these measurements) required in order to obtain subkilometer structures is impractical. It is conceivable that with a near-perfect $\mathbf{S}_a$ matrix a reasonable solution could be obtained, but that shifts the problem to the derivation of a perfect a priori.

To better estimate $\mathbf{S}_a$, another source of information is needed. We chose to consider synergetic measurements of the tomographic MWR measurements and of a set of vertical profiles by an RL to improve the retrieval of the 2D water vapor field. We shall use the RL in several different ways in the retrieval, including using the RL measurements of the true fields in order to constrain the $\mathbf{S}_a$ matrix. The retrieval of the spatially

smoother wedge field yielded better results relative to the retrieval in the alternating blob case because it has less small-scale variability; thus, we continue examining only the more challenging alternating blob field.

a. Raman lidar characteristics and setup

Using the findings of section 3, we will limit the use of the MWR to the HATPRO radiometer with 25 elevation angles. We will continue to use a different number of instruments, namely, one, two, and five MWRs. In this section, the synergetic measurements are done using both MWRs and an RL. Although five MWRs cost about the same as one RL, we will only examine the case combining both type of instruments, since the improvement of the tomographic measurements is the goal of this paper.

The RL was placed at three different locations in this field in order to evaluate the impact of having the direct water vapor vertical profile measurements from the lidar on the retrieved 2D solution. The three locations of the lidar were in the center of the field (i.e., 14.4 km from the edge of the domain, as the domain is 28.8 km wide), on the right of the field (6.4 km from the edge of the domain), and in between these two locations (10.4 km from the edge of the domain).

b. Raman lidar simulator

The forward model was modified so that it calculates the resulting measurements for both the scanning MWRs and the RL. The integration time of the RL instrument simulator is assumed to be 50 s to be compatible with the scanning time of a HATPRO MWR for 25 elevation angles (2 s per angle). The RL measures vertical profiles of humidity in time as the humidity field advects over the lidar.

Here, we assume a $6\,\mathrm{m\,s^{-1}}$ wind, which is a typical value for the area around the ARM SGP site (Luna and Church 1974) and is moving the true water vapor field blowing along the MWR observation axis, and thus the 50-s integration time for the RL yields a displacement of the water vapor field of 300 m during this period. Once the horizontal displacement is found, it is distributed equally around the location of the RL (i.e., from the previous case, 150 m each side of the location of the RL). The water vapor profiles included in this horizontal displacement are used to create the RL measurements. For each of these profiles, the water vapor profiles of the true atmosphere for that profile is taken and a Gaussian-distributed random noise with a magnitude of the RL errors is added to each level of that profile (Fig. 8). The profiles with the noise introduced are used to simulate the RL measurements.

The RL measurements are added to the observational vector unless otherwise specified. In addition, the Jacobian

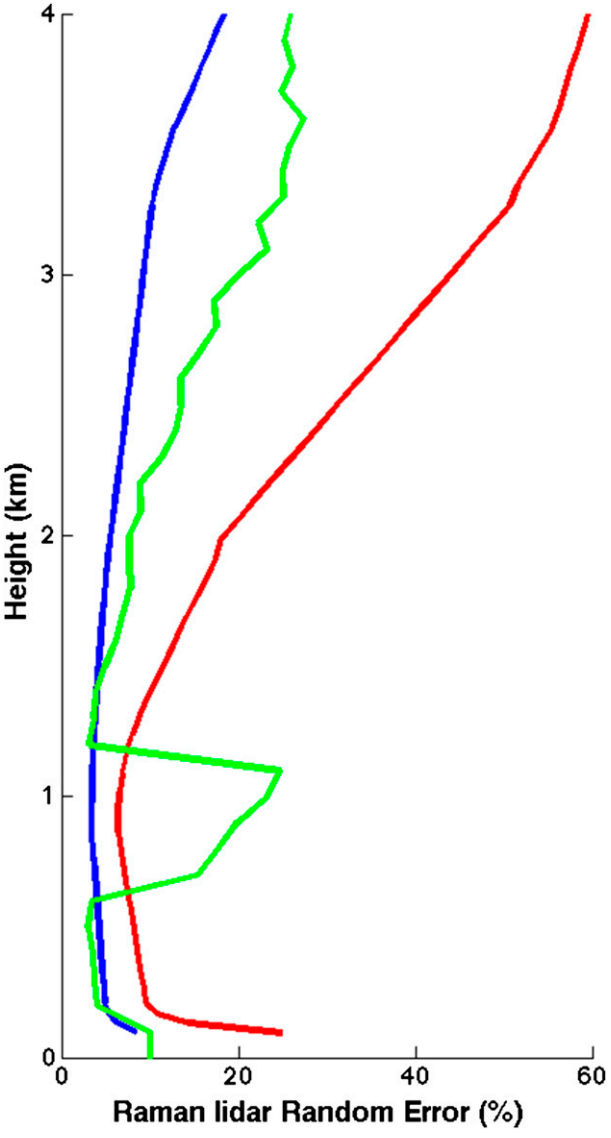

FIG. 8. Mean fractional error (percent of water vapor mixing ratio) of the Raman lidar for data integrated over 10 s at 75-m resolution on 23 Sep 2006 at the Department of Energy's ARM SGP site near Lamont. Blue and red traces are the nighttime and daytime errors, respectively. In this study, the high-resolution daytime errors are used. RL-observed variance of the field is used to create the representativeness errors for the alternating blobs (green).

is set to 1, because a perturbation in the field yields the same perturbation in the RL's measurements (i.e., we are assuming that the RL has perfect sensitivity to fluctuations of water vapor in the atmosphere). The $\mathbf{S}_\varepsilon$ matrix is still a diagonal matrix with the instrument error variances on the diagonal elements. The MWR error is 0.7 K as was used previously. The RL errors were created by multiplying the fractional error (Fig. 8) by the true field. The fractional errors of the RL are derived

from 10-s median values from the RL situated at the ARM SGP site near Lamont, Oklahoma, on 23 September 2006 (Fig. 8, red and blue). In this study, the daytime fractional error profile (red curve) is used. These errors were interpolated to the vertical grid of the water vapor field used in this study (surface to 7 km AGL). At the very lowest vertical level and for levels above 5 km, the errors were increased to reflect the uncertainties in the RL at very low and very high levels in the atmosphere.

c. *Simulation experiments: Varying the use of Raman lidar data*

Several different methods of incorporating the RL into the optimal estimation framework were investigated: 1) including the RL observations in the observation vector used by the retrieval, 2) using the variance of a field observed by the RL over time to define the representativeness errors, 3) using the temporal mean of the field observed by the RL to define the a priori field (i.e., $\boldsymbol{X}_a$) of the retrieval, and 4) using a field observed by the RL over time to define the $\boldsymbol{X}_a$ field and its covariance $\mathbf{S}_a$. These are discussed in the following sections.

When the RL is used in the observation vector with the original $\mathbf{X}_a$ vector, $\mathbf{S}_a$ matrix, and $\mathbf{S}_\varepsilon$ matrix, there is negligible improvement in the RMSD and the gain in DFS of adding the RL is equivalent to adding an additional 1.5 MWRs to the retrieval. In fact, the decrease in RMSD is only slightly smaller than the case when only MWRs are used in the retrieval. In addition, the vertical variability profile was not improved. Thus, the benefit of incorporating the RL measurements into the retrieval in this manner is minimal. It should be noted that in this test we are comparing simultaneous measurements of the RL and the full scans of the MWR, which took 50 s. Although the results from the Raman lidar are indeed better and have more resolution, the Raman lidar only provided information over one column in this setup, thus "limiting" the number of DFS to one per level with RL measurements. On the other hand, the radiometers were scanning through the atmospheric field. In the context of a horizontal error correlation distance of 13.5 km (that of the original non-RL $\mathbf{S}_a$ matrix), this means that a scanning radiometer can obtain several nearly independent constraints over many directions, bringing their DFS to more than half a Raman lidar in this context.

Previously, the $\mathbf{S}_\varepsilon$ matrix had no information on the representativeness errors; the errors included in this matrix were solely the uncertainties' instrument measurements. However, in addition to the uncertainties in the observations themselves, there are also errors associated with the forward model that can include many different components: uncertainties in other input variables needed by the model that are not in the state vector $\mathbf{X}$, model parameters, and sampling or representativeness errors. Here, we examined the utility of adding the representativeness errors to the observational errors in the tomographic retrieval. Essentially, the representativeness error is the error made by assuming that a measurement at a point in space can be applied to the surrounding points. The representativeness errors $\mathbf{S}_r$ were added to both the MWR and the RL (Fig. 8), and both these instruments were used in the $\mathbf{S}_\varepsilon$ matrix as such:

$$\mathbf{S}_\varepsilon = \mathbf{S}_y + \mathbf{K}\mathbf{S}_r\mathbf{K}^{\mathrm{T}}, \tag{8}$$

where $\mathbf{S}_y$ is the instrument's error variance used to define the $\mathbf{S}_\varepsilon$ matrix in section 2b. The DFS decreased by about 50% when the representativeness error was included in the retrieval via $\mathbf{S}_\varepsilon$ compared to when the $\mathbf{S}_r$ matrix was not included. The change in the RMSD when the representativeness error was included, relative to when it was not, was negligible. Therefore, the solutions that included the observation representativeness errors were not significantly improved compared to the solutions that did not include these errors.

The previously described two methods of including RL did not greatly improve the retrieval, demonstrating that constraining the vertical profile and the observation errors are insufficient. We will now use the field measured by the RL to provide the a priori information. In this experiment, we take the 1-h average profile from the RL observations and use this profile for all columns of the new a priori field $\mathbf{X}_a$. As such, the new a priori field is still vertically stratified and horizontally homogeneous, but with the correct average value and the correct BL height. Since the RL was used as previous knowledge to derive the a priori, it was not used in $\mathbf{Y}$ as current knowledge of the field. Therefore, the observation vector consisted solely of observations from the MWRs, as such the representativeness errors are only included for the MWR instruments. In addition, the $\mathbf{S}_a$ matrix and the Jacobian matrix are the ones described in section 2b. Most of the solution fields look qualitatively similar to the a priori field, especially when a small number of instruments are used. The field starts to show more structure when five MWRs are used to measure the field (Fig. 9). The RMSD is decreased by a factor of 1.2 when the RL is used to define the a priori compared to when only MWRs are used to measure the field (Table 1). There is no significant improvement in the shape or magnitude of the vertical profile of variability between using only MWRs and using the RL to define the a priori field (Fig. 10, red) versus using only five MWRs with the original $\mathbf{X}_a$ (Fig. 10, purple).

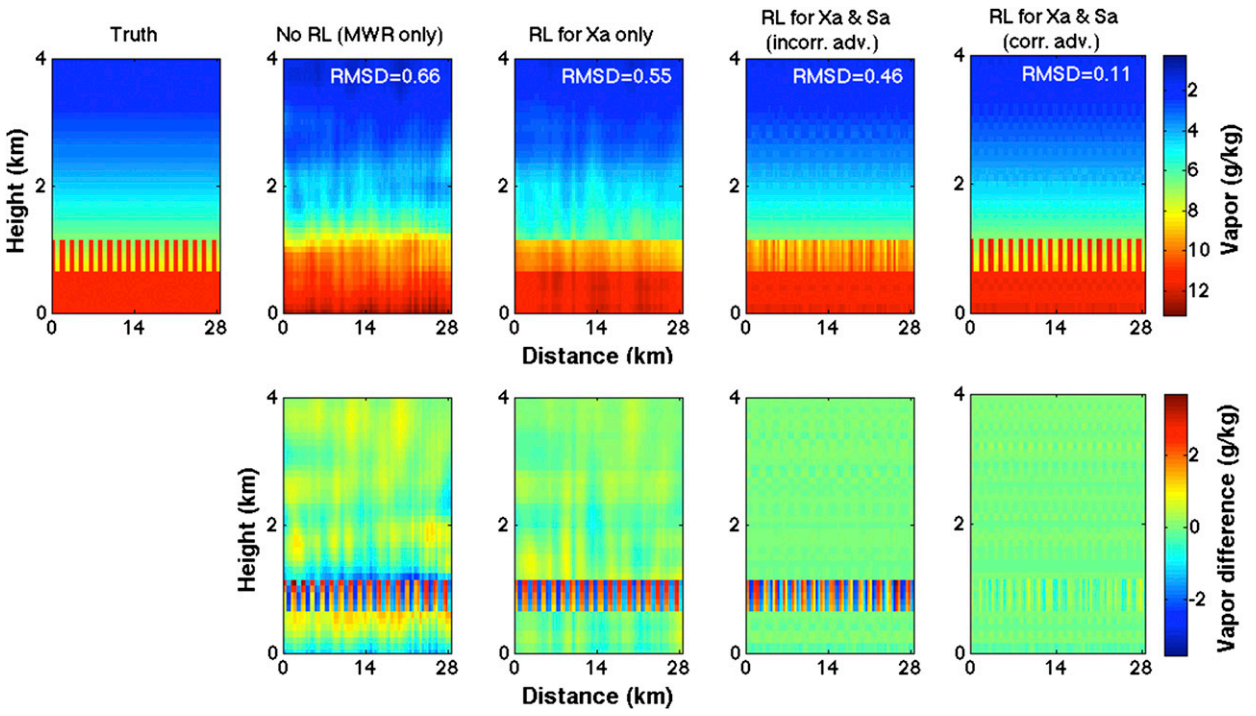

FIG. 9. (top) Comparison of resulting fields and RMSD (g kg^{-1}) between the true water vapor field: (left to right) using only the MWR, using the RL to define the $\mathbf{X}_a$ only, using the RL to define the $\mathbf{X}_a$ vector and the $\mathbf{S}_a$ matrix with incorrect advection, and using the RL to find the $\mathbf{X}_a$ vector and the $\mathbf{S}_a$ matrix with correct advection. All panels (other than the truth) use observations from five HATPRO radiometers with 25 elevation angles. (bottom) Difference between the solution and the truth fields for the same cases as in (top).

The final way to include the RL in the retrieval is to use the 1-h time series of RL observations described in the previous section, not only to obtain a good mean a priori field $\mathbf{X}_a$ but also to compute the $\mathbf{S}_a$ matrix. Here again, the observation vector $\mathbf{Y}$ only contains measurements from the MWR and as such $\mathbf{S}_\varepsilon$ only includes the errors for these instruments. The RMSD was the lowest of all the retrievals of this study. Given that the RMSD between the a priori and the truth was 0.86 g kg^{-1} for all simulations (Fig. 6, dashed line), we used that as a basis to evaluate the performance of the retrieval. For example, using five MWRs with the original $\mathbf{S}_a$ matrix and $\mathbf{X}_a$ vector yielded an RMSD of 0.66 g kg^{-1}, which decreased to 0.55 when RL time series is used to define the mean a priori $\mathbf{X}_a$ (Table 1; Fig. 9). However, using the $\mathbf{X}_a$ and $\mathbf{S}_a$ matrix derived from the RL time series gives an RMSD of 0.11 g kg^{-1}, a factor-of-6 improvement (Table 1; Fig. 9). This demonstrates the importance that the $\mathbf{S}_a$ matrix plays in the retrieval and how a more accurate specification of this matrix improves the quality of the retrieval. Note, in particular, that the height and shape of the water vapor field in the boundary layer is similar to the truth (Fig. 9). The magnitude of the variability approaches that of the truth field as the number of MWRs increases; however, even using five MWRs, the magnitude is still slightly underestimated (Fig. 10, green).

The success of this technique compared to the previous methods investigated in this study lies in the definition of the $\mathbf{S}_a$ matrix. In this case, the $\mathbf{S}_a$ matrix was created from RL measurements and reflected the covariance in the atmosphere perfectly (i.e., no evolution in the atmosphere and the advection is well captured). In other words, we have assumed Taylor's frozen turbulence hypothesis. To investigate the effect of an error in advection, another mean a priori field and $\mathbf{S}_a$ matrix were created using RL observations. This time the horizontal advection was slowed such that the blobs in the RL field were 1.5 times the size of those in the truth field (i.e., the advection is slower by 33%); this case will be referred to as the "incorrect advection" blobs (Figs. 9 and 10, blue), whereas the case where the advection was correctly assumed is the "correct advection" blob case (Figs. 9 and 10, green). The differences between the two a priori fields are negligible. Therefore, the main difference is the covariance in the $\mathbf{S}_a$ matrix.

The results that used the incorrect advection to define $\mathbf{S}_a$ were not as impressive as the previous ones done with the correct advection $\mathbf{S}_a$ matrix, as the individual blobs were not resolved (Fig. 9) but were better than using the

TABLE 1. RMSD values in mixing ratio ($g\,kg^{-1}$) for the alternating blob where the specified $\mathbf{X}_a$ and $\mathbf{S}_a$ data were used in an MWR tomographic retrieval using 25 elevation angles. A number of MWRs (columns) were used in the retrieval. Note that the RMSD between the true field and the a priori field is $0.86\,g\,kg^{-1}$ for all cases.

	1 MWR	2 MWRs	5 MWRs
No RL and original $\mathbf{X}_a$ and $\mathbf{S}_a$ matrix	0.67	0.63	0.66
Using RL-derived $\mathbf{X}_a$ and original $\mathbf{S}_a$ matrix	0.61	0.56	0.55
Using RL-derived $\mathbf{X}_a$ and $\mathbf{S}_a$ matrix where advection was incorrectly specified when computing $\mathbf{S}_a$	0.52	0.51	0.46
Using RL-derived $\mathbf{X}_a$ and $\mathbf{S}_a$ matrix where advection was correctly specified when computing $\mathbf{S}_a$	0.19	0.16	0.11

RL to define the $\mathbf{X}_a$ while using the original $\mathbf{S}_a$ matrix (Fig. 9). The variability of the retrieved field still captures the height and shape of the vertical variability profile, but the magnitude of the variability is smaller than when the $\mathbf{S}_a$ matrix was created using the correct advection blobs (green vs blue lines in Fig. 10).

Finally, the RMSD is also larger in this case than with the correct advection $\mathbf{S}_a$ matrix. Using this incorrect advection $\mathbf{S}_a$ matrix, but which is probably more realistic in actual practice, yielded a solution that was 4 times worse in RMSD than that with the correct advection $\mathbf{S}_a$ matrix, but 1.3 times better than that with the original $\mathbf{X}_a$ vector and $\mathbf{S}_a$ matrix and 1.2 times better than using the RL to define $\mathbf{X}_a$ vector and the original $\mathbf{S}_a$ matrix (Table 1). This further illustrates the sensitivity of the final solution to the quality of $\mathbf{S}_a$, when even if $\mathbf{S}_a$ was derived from perfect data but using an imperfect translational velocity (or when the Taylor's hypothesis is not valid), the retrieval fails to deliver good results. Here, we examined a simple error in advection velocity: should $\mathbf{S}_a$ be derived from perfect data but with more complex errors in winds than a simple bias, the results would probably be worse.

5. Conclusions

This observation system simulation experiment was done to quantify the changes in degrees of freedom for signal (DFS) and the accuracy of a tomographic retrieval of a 2D water vapor field in the boundary layer for various microwave radiometer (MWR) tomographic setups and when using a Raman lidar (RL) in synergy with the MWRs. An optimal-estimation-based methodology was applied to two atmospheric cases—an alternating blob and a wedge pattern (Fig. 2)—to test the ability of the tomographic approach to retrieve the water vapor field in different conditions. The alternating blob represents a turbulent afternoon boundary layer with plumes of moisture penetrating the top of the boundary layer (in an exaggerated way), while the wedge represents the passage of a water vapor front (e.g., dryline or cold front).

We first examined the effects of the MWR configuration, such as the number of elevation angles, frequencies, and instruments. We found that increasing the number of MWRs and elevation angles yielded the largest increase of DFS, which is consistent with the idea behind tomographic measurements. Although increasing the number of measurement while using a generic a priori covariance matrix ($\mathbf{S}_a$) yielded good results for the smoother wedge atmosphere, the more complex alternating blob field was not retrieved as well, mainly because the subkilometer-scale features were not resolved. When the vertical and horizontal correlation distances of the $\mathbf{S}_a$ matrix were reduced, the retrieved field did capture more of the small-scale features, but the magnitude, the location of the maximum variability of the field, and the shape of the horizontal mean were not well captured. Finally, we added an RL to the MWR tomographic measurements and used it in different ways in the retrieval, including using RL time series observations to define the a priori field ($\mathbf{X}_a$) and the $\mathbf{S}_a$ matrix correlation lengths. When the RL was used to define only the mean $\mathbf{X}_a$ and the generic $\mathbf{S}_a$ matrix was used in the retrieval, the solution captured the location of the BL top correctly because it was constrained by the RL, but the solution field did not capture the alternating blobs in the BL nor did it capture the magnitude and shape of the variability of the true field. However, when the $\mathbf{S}_a$ matrix was derived from the RL time series where the horizontal advection speed was accurate, the solutions captured the subkilometer-scale features in the observed field and placed them at the correct location. On the other hand, when the $\mathbf{S}_a$ matrix was derived from the RL observations with an error in the advection velocity, the solutions were not capable of placing the subkilometer-scale feature at the correct location, but they did have the boundary layer height correct and more accurately captured the vertical location of the largest variability. The magnitude of the variability was correctly placed in the vertical profile but is underestimated in both cases.

Our findings suggest that the capacity of the tomographic retrieval to capture subkilometer scale, especially in the vertical, depends mainly on the definition of the

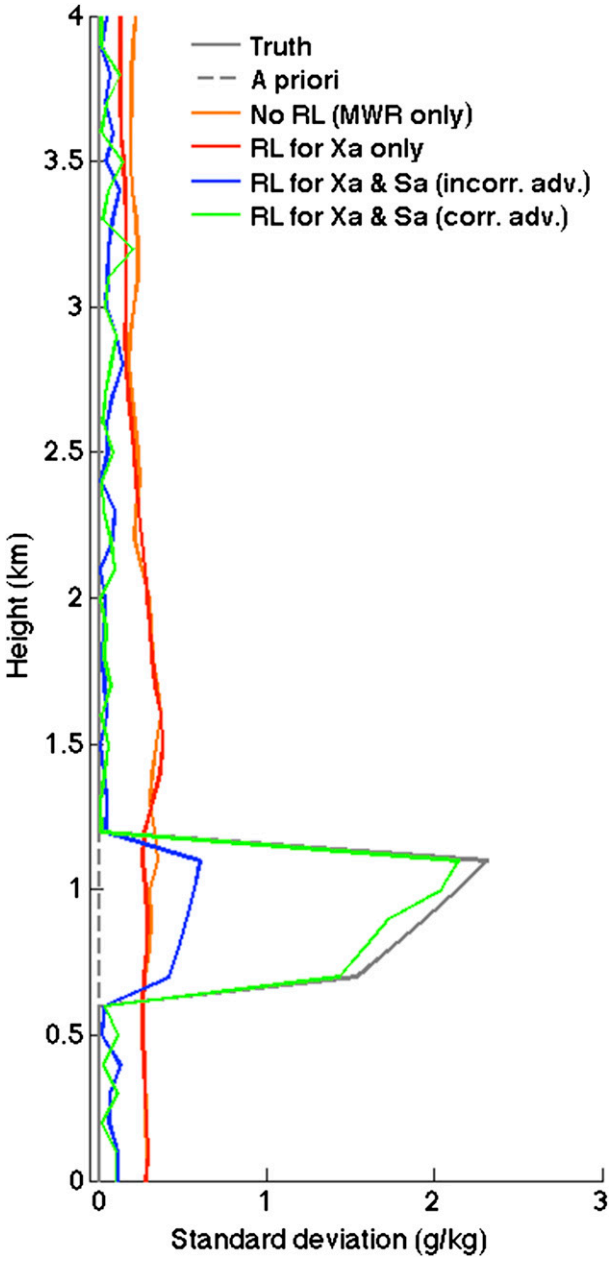

FIG. 10. Horizontal standard deviation profile for solutions without RL (orange), with RL used to define the a priori (red), with RL used to define the $\mathbf{S}_a$ matrix with incorrect advection (blue), with RL used to define the $\mathbf{S}_a$ matrix with correct advection (green), the a priori field (dashed gray), and the true field (solid gray) for the alternating blobs water vapor atmosphere. Solutions used observations from five MWRs in the retrieval.

$\mathbf{S}_a$ matrix. Not only does the $\mathbf{S}_a$ matrix need to be accurate for the field, but errors of displacement or translation velocity when deriving the correlations used in the matrix can impact the solution negatively; adding instruments and elevation angles does not mitigate this problem significantly.

Acknowledgments. The funding for this project was provided by the National Sciences and Engineering Research Council of Canada and from the Fonds de la Recherche du Québec sur la Nature et les Technologies. We thank Adam Clark (National Severe Storm Laboratory and Cooperative Institute for Mesoscale Meteorological Studies) and Fanyou Kong (Center for Analysis and Prediction of Storms, Oklahoma University) for their help in determining the horizontal correlation length scale from a series of 1-km-resolution WRF simulations. We thank the National Severe Storm Laboratory for supporting the first author's visit to its offices in Norman, OK, in September 2011. We thank the McGill Marshall Radar Observatory for the use of its computers for the time of this project. Finally, we also thank our colleagues in the Integrated Remote Sensing research group at Cologne University and Frédéric Fabry at McGill University for discussions related to this paper.

REFERENCES

Bean, B. R., and E. J. Dutton, 1966: *Radio Meteorology*. U.S. Government Printing Office, 435 pp.

Bevis, M., S. Businger, T. A. Herring, C. Rocken, R. A. Anthes, and R. H. Ware, 1992: GPS meteorology: Remote sensing of atmospheric water vapor using global positioning system. *J. Geophys. Res.,* **97,** 15 787–15 801, doi:10.1029/92JD01517.

Bobylev, L. P., 1997: Retrieval of liquid water distribution in convective clouds using microwave computerized tomography. *IGARSS '97: 1997 IEEE International Geoscience and Remote Sensing Symposium; Remote Sensing—A Scientific Vision of Sustainable Development,* T. I. Stein, Ed., Vol. 2, IEEE, 830–832.

Cadeddu, M. P., J. C. Liljegren, and D. D. Turner, 2013: The Atmospheric Radiation Measurement (ARM) program network of microwave radiometers: Instrumentation, data, and retrievals. *Atmos. Meas. Tech. Discuss.,* **6,** 3723–3763, doi:10.5194/amtd-6-3723-2013.

Crewell, S., and U. Löhnert, 2003: Accuracy of cloud liquid water path from ground-based microwave radiometry 2. Sensor accuracy and synergy. *Radio Sci.,* **38,** 8042, doi:10.1029/2002RS002634.

Drake, J. F., and J. Warner, 1988: A theoretical study of the accuracy of tomographic retrieval of cloud liquid with an airborne radiometer. *J. Atmos. Oceanic Technol.,* **5,** 844–856, doi:10.1175/1520-0426(1988)005<0844:ATSOTA>2.0.CO;2.

Ferrare, R. A., and Coauthors, 2006: Evaluation of daytime measurements of aerosols and water vapor made by an operational Raman lidar over the Southern Great Plains. *J. Geophys. Res.,* **111,** D05S08, doi:10.1029/2005JD005836.

Fleming, H. E., 1982: Satellite remote sensing by the technique of computed tomography. *J. Appl. Meteor.,* **21,** 1538–1549, doi:10.1175/1520-0450(1982)021<1538:SRSBTT>2.0.CO;2.

Goldsmith, J. E. M., F. H. Blair, S. E. Bisson, and D. D. Turner, 1998: Turn-key Raman lidar for profiling atmospheric water vapor, clouds, and aerosols. *Appl. Opt.,* **37,** 4979–4990, doi:10.1364/AO.37.004979.

Han, Y., and E. R. Westwater, 1995: Remote sensing of tropospheric water vapor and cloud liquid water by integrated

ground-based sensors. *J. Atmos. Oceanic Technol.,* **12,** 1050–1059, doi:10.1175/1520-0426(1995)012<1050:RSOTWV>2.0.CO;2.

——, J. B. Snider, E. R. Westwater, S. H. Mefi, and R. A. Ferrare, 1994: Observations of water vapor by ground-based microwave radiometers and Raman lidar. *J. Geophys. Res.,* **99,** 18 695–18 702, doi:10.1029/94JD01487.

Hardesty, R. M., and R. M. Hoff, Eds., 2012: Thermodynamic Profiling Technologies Workshop report to the National Science Foundation and the National Weather Service. NCAR Tech. Note NCAR/TN-488+STR, 80 pp.

Huang, D., Y. Liu, and W. Wiscombe, 2008: Determination of cloud liquid water distribution using 3D cloud tomography. *J. Geophys. Res.,* **113,** D13201, doi:10.1029/2007JD009133.

——, A. Gasiewski, and W. Wiscome, 2010: Tomographic retrieval of cloud liquid water fields from a single scanning microwave radiometer aboard a moving platform—Part 1: Field trial results from the Wakasa Bay experiment. *Atmos. Chem. Phys.,* **10,** 6685–6697, doi:10.5194/acp-10-6685-2010.

Iturbide-Sanchez, F., S. C. Reising, and S. Padmanabhan, 2007: A miniaturized spectrometer radiometer based on MMIC technology for tropospheric water vapor profiling. *IEEE Trans. Geosci. Remote Sens.,* **45,** 2181–2194, doi:10.1109/TGRS.2007.898444.

Liebe, H. J., 1989: MPM—An atmospheric millimeter-wave propagation model. *J. Infrared and Mill. Waves,* **10,** 631–650, doi:10.1007/BF01009565.

Löhnert, U., S. Crewell, and C. Simmer, 2004: An integrated approach toward retrieving physically consistent profiles of temperature, humidity, and cloud liquid water. *J. Appl. Meteor.,* **43,** 1295–1307, doi:10.1175/1520-0450(2004)043<1295:AIATRP>2.0.CO;2.

——, D. D. Turner, and S. Crewell, 2009: Ground-based temperature and humidity profiling using spectral infrared and microwave observations. Part I: Simulated retrieval performance in clear-sky conditions. *J. Appl. Meteor. Climatol.,* **48,** 1017–1032, doi:10.1175/2008JAMC2060.1.

Luna, R. E., and H. W. Church, 1974: Estimation of long-term concentrations using a ''universal'' wind speed distribution. *J. Appl. Meteor.,* **13,** 910–916, doi:10.1175/1520-0450(1974)013<0910:EOLTCU>2.0.CO;2.

Masutani, M., and Coauthors, 2010: Observing system simulation experiments. *Data Assimilation: Making Sense of Observations,* W. A. Lahoz, B. Khatattov, and R. Ménard, Eds., Springer, 647–679.

Meunier, V., U. Löhnert, P. Kollias, and S. Crewell, 2013: Biases caused by the instrument bandwidth and beam width on simulated brightness temperature measurements from scanning microwave radiometers. *Atmos. Meas. Tech.,* **6,** 1171–1187, doi:10.5194/amt-6-1171-2013.

Padmanabhan, S., S. C. Reising, J. Vivekanandan, and F. Iturbide-Sanchez, 2009: Retrieval of atmospheric water vapor density with fine spatial resolution using three-dimensional tomographic inversion of microwave brightness temperatures measured by a network of scanning compact radiometers. *IEEE Trans. Geosci. Remote Sens.,* **47,** 3708–3721, doi:10.1109/TGRS.2009.2031107.

Radiometer Physics GmbH, 2011: Technical instrument manual: Description of instrument technology. Radiometer Physics GmbH Rep. RPG-MWR-STD, 45 pp. [Available online at http://www.radiometer-physics.de/rpg/html/docs/RPG_MWR_STD_Technical_Manual.pdf.]

Rodgers, C. D., 2000: *Inverse Methods for Atmospheric Sounding: Theory and Practice.* World Scientific, 238 pp.

Rosenkranz, P. W., 1998: Water vapor microwave continuum absorption: A comparison of measurements and models. *Radio Sci.,* **33,** 919–928, doi:10.1029/98RS01182.

Schween, J. H., S. Crewell, and U. Löhnert, 2011: Horizontal-humidity gradient from one single-scanning microwave radiometer. *IEEE Geosci. Remote Sens. Lett.,* **8,** 336–340, doi:10.1109/LGRS.2010.2072981.

Steinke, S., U. Löhnert, S. Crewell, and S. Lui, 2014: Water vapor tomography with two microwave radiometers. *IEEE Geosci. Remote Sens. Lett.,* **11,** 419–423, doi:10.1109/LGRS.2013.2264354.

Stokes, G. M., and S. E. Schwartz, 1994: The Atmospheric Radiation Measurement (ARM) Program: Programmatic background and design of the cloud and radiation test bed. *Bull. Amer. Meteor. Soc.,* **75,** 1201–1221, doi:10.1175/1520-0477(1994)075<1201:TARMPP>2.0.CO;2.

Turner, D. D., and J. E. M. Goldsmith, 1999: Twenty-four Raman lidar water vapor measurements during the Atmospheric Radiation Measurement Program's 1996 and 1997 water vapor intensive observation periods. *J. Atmos. Oceanic Technol.,* **16,** 1062–1076, doi:10.1175/1520-0426(1999)016<1062:TFHRLW>2.0.CO;2.

——, W. F. Feltz, and R. A. Ferrare, 2000: Continuous water vapor profiles from operational ground-based active and passive remote sensors. *Bull. Amer. Meteor. Soc.,* **81,** 1301–1317, doi:10.1175/1520-0477(2000)081<1301:CWBPFO>2.3.CO;2.

——, S. A. Clough, J. C. Liljegren, E. E. Clothiaux, K. Cady-Pereira, and K. L. Gaustad, 2007: Retrieving liquid water path and precipitable water vapor from Atmospheric Radiation Measurement (ARM) microwave radiometers. *IEEE Trans. Geosci. Remote Sens.,* **45,** 3680–3690, doi:10.1109/TGRS.2007.903703.

——, M. P. Cadeddu, U. Löhnert, S. Crewell, and A. M. Vogelmann, 2009: Modifications to the water continuum in the microwave suggested by ground-based 150-GHz observations. *IEEE Trans. Geosci. Remote Sens.,* **47,** 3326–3109, doi:10.1109/TGRS.2009.2022262.

Warner, J., J. F. Drake, and P. R. Krehbiel, 1985: Determination of cloud liquid water distribution by inversion of radiometric data. *J. Atmos. Oceanic Technol.,* **2,** 293–303, doi:10.1175/1520-0426(1985)002<0293:DOCLWD>2.0.CO;2.

——, ——, and J. B. Snider, 1986: Liquid water distribution obtained from coplanar scanning radiometers. *J. Atmos. Oceanic Technol.,* **3,** 542–546, doi:10.1175/1520-0426(1986)003<0542:LWDOFC>2.0.CO;2.

Weckwerth, T. M., V. Wulfmeyer, R. M. Wakimoto, R. M. Hardesty, J. W. Wilson, and R. M. Banta, 1999: NCAR–NOAA lower-tropospheric water vapor workshop. *Bull. Amer. Meteor. Soc.,* **80,** 2339–2357, doi:10.1175/1520-0477(1999)080<2339:NNLTWV>2.0.CO;2.

Wulfmeyer, V., and J. Bösenberg, 1998: Ground-based differential absorption lidar for water-vapor profiling: Assessment of accuracy, resolution, and meteorological applications. *Appl. Opt.,* **37,** 3825–3844, doi:10.1364/AO.37.003825.

——, S. Pal, D. D. Turner, and E. Wagner, 2010: Can water vapor Raman lidar resolve profiles of turbulent variables in the convective boundary layer? *Bound.-Layer Meteor.,* **136,** 253–284, doi:10.1007/s10546-010-9494-z.